Article

Current Biology

A spinal circuit for skilled locomotion

Highlights

- Identification of glutamatergic Pitx2^{+} V0 ascending neurons (V0g-aNs)
- V0g-aNs are integrated into spinal sensorimotor circuits
- V0g-aNs are not needed for interlimb coordination but are required for skilled locomotion

Authors

Elisa Toscano, Nadezhda Evtushenko, Maddalena Giomi, ..., Aristotelis Misios, Carmen Birchmeier, Niccolò Zampieri

Correspondence

niccolo.zampieri@mdc-berlin.de

In brief

Toscano et al. identify glutamatergic Pitx2^{+} V0 ascending neurons (V0g-aNs) that receive input from cerebrospinal fluid (CSF)-contacting neurons and target spinal premotor and motor neurons. Elimination of V0g-aNs does not affect gait generation or transition but selectively impairs the execution of more challenging tasks, revealing a circuit dedicated to skilled locomotion.

Toscano et al., 2025, Current Biology *35*, 1–12
October 20, 2025 © 2025 The Author(s). Published by Elsevier Inc.
https://doi.org/10.1016/j.cub.2025.09.030

CellPress

Please cite this article in press as: Toscano et al., A spinal circuit for skilled locomotion, Current Biology (2025), https://doi.org/10.1016/j.cub.2025.09.030

Current Biology

CellPress
OPEN ACCESS

Article

A spinal circuit for skilled locomotion

Elisa Toscano,[1] Nadezhda Evtushenko,[1] Maddalena Giomi,[1] Alessandro Santuz,[1] Philine Thieme,[1] Elijah David Lowenstein,[2] Aristotelis Misios,[2] Carmen Birchmeier,[2,3] and Niccolò Zampieri[1,4,*]

[1]Laboratory of Development and Function of Neural Circuits, Max Delbrück Center for Molecular Medicine, Robert-Rössle-Str. 10, 13125 Berlin, Germany

[2]Laboratory of Developmental Biology/Signal Transduction, Max Delbrück Center for Molecular Medicine, Robert-Rössle-Str. 10, 13125 Berlin, Germany

[3]Neurowissenschaftliches Forschungzentrum, NeuroCure Cluster of Excellence, Charité, Charitéplatz 1, 10117 Berlin, Germany

[4]Lead contact

*Correspondence: niccolo.zampieri@mdc-berlin.de

https://doi.org/10.1016/j.cub.2025.09.030

SUMMARY

Neural circuits in the spinal cord have a critical role in integrating sensory information and descending commands to coordinate body movements. Defining the functional diversity of spinal neurons is therefore essential for understanding the mechanisms underlying motor control. In this study, by combining anatomical, molecular, and functional analyses in mice, we identified and characterized a subtype of spinal ascending neurons belonging to the V0 family. We found that V0g ascending neurons are integrated in lumbar sensorimotor circuits, and their function is specifically required for the execution of precise limb movements necessary for skilled locomotion. This work advances our understanding of the functional organization of V0 neurons and highlights a previously unappreciated role in adjusting body movements to the more demanding needs of skilled locomotor tasks.

INTRODUCTION

The remarkable repertoire of animal behaviors relies on the ability of the nervous system to effortlessly orchestrate the movement of different parts of the body.[1] Spinal neurons are a key component of motor circuits integrating descending commands and sensory information to regulate the concerted activation of muscles controlling limb movements and body posture. Precise control of the rhythm and pattern of muscle activation is critical for adapting to the specific requirements of different locomotor tasks. For example, to increase speed, quadrupedal animals transition from gaits characterized by alternation of left-right limb movement (i.e., walk and trot) to gaits favoring synchronous activation (i.e., half-bound and bound).[2] Several classes of spinal neurons have been shown to participate in the coordination of limb movements. In particular, specialized neural networks located within the spinal cord—the central pattern generators (CPGs)—can autonomously generate rhythmic patterns of muscle contraction that underlie stereotyped locomotor movements such as walking and running.[3] CPGs are composed of multiple neuronal subtypes that are arranged in functional modules with specific positional organization (i.e., segmental, cervical vs. lumbar) and connectivity (i.e., unilateral vs. bilateral and local vs. long distance) to hierarchically control fundamental features of motor control such as coordination of joint (i.e., flexor-extensor alternation) and limb (i.e., left-right and forelimb-hindlimb alternation) movements. In addition, CPGs are strongly modulated by descending input and sensory information, which adjust basic rhythmic patterns and produce skilled movements that are necessary for adapting to more demanding conditions like walking on a beam.[4]

The cardinal classes of V0 and V2a spinal neurons play a central role in controlling left-right alternation.[5–7] In the absence of V0 neurons, mice do not alternate left and right limbs but instead use a synchronous bound gait at all speeds.[2] Moreover, the inhibitory (V0d) and excitatory (V0v) subsets have been shown to have distinct roles. V0d neurons secure alternating limb movements at low speeds, whereas excitatory V0v controls coordination at high speeds.[2,5] Similarly, V2a neurons have been shown to selectively contribute to maintaining left-right alternation at high speeds.[8] In addition, propriospinal neurons—neurons interconnecting different segments of the spinal cord—are known to participate in the control of limb coordination.[9] Propriospinal neurons can be categorized into distinct subtypes based on cell body position, axonal length, and projection pattern.[10] Long descending and ascending neurons (dNs and aNs) reciprocally connect the cervical and lumbar enlargements, and selective perturbation of their function has proven their importance in interlimb coordination.[11,12] Elimination of dNs in mice results in altered hindlimb coordination during fast-paced treadmill locomotion.[11] Reversible silencing of aNs in rats disrupts left-right alternation at both forelimb and hindlimb levels, as well as contralateral hindlimb-forelimb coordination.[12] Despite their importance, the molecular diversity of propriospinal neurons remains unclear. Little is known about aNs identity aside from a recently identified subset of V3 neurons.[13] dNs include subsets of V0 and V2a neurons.[11,14] At the functional level, the contributions of propriospinal neuron subtypes to locomotor control have not yet been elucidated. Here, we combined viral tracing and transcriptomics to identify an ascending population of neurons innervating the cervicalspinal cord and the brainstem that belongs to the glutamatergic subset of the Pitx2^{+} V0 family

This is an open access article under the CC BY license (http://creativecommons.org/licenses/by/4.0/).

Please cite this article in press as: Toscano et al., A spinal circuit for skilled locomotion, Current Biology (2025), https://doi.org/10.1016/j.cub.2025.09.030

(V0g-aNs).[15,16] We found that V0g-aNs are integrated into spinal sensorimotor circuits, sending output to premotor and motor neurons and receiving input from cerebrospinal fluid-contacting neurons (CSF-cNs)—intraspinal sensory neurons monitoring CSF composition and flow that have important roles in the control of skilled locomotion in mice.[17,18] Selective elimination of V0g-aNs does not affect interlimb coordination or speed-dependent gait control but specifically perturbs the ability to walk on a ladder or a beam. These results provide new insights into the functional organization of V0 neurons and identify V0g-aNs as a key component, along with CSF-cNs, of a spinal sensorimotor circuit that adjusts limb and body movements to the more complex demands of skilled locomotion.

RESULTS

Anatomical characterization of long ascending and descending neurons

To label neurons reciprocally connecting limb levels of the spinal cord, we took advantage of the retrograde tracing properties of the rabies virus.[19] We unilaterally injected G-deleted rabies virus (SAD B19)[19] encoding a nuclear localized fluorescent protein (RVΔG H2B-mCherry) into either the lumbar (L) or cervical (C) spinal cord of post-natal days (P) 5–8 mice to visualize dNs and aNs (Figures 1A–1D). We chose to inject at the L3-L4 and C6-C7 levels, as these spinal segments are known to contain the primary centers for locomotor-like rhythmogenesis.[12,20] To assess dNs and aNs abundance and distribution, we counted labeled nuclei and reconstructed their positional organization (Figures 1E, S1, and S2; Table S1). We observed that the majority of aNs exhibit contralateral connectivity (27%–73% ipsi-contra), while dNs have a larger ipsilateral component (42%–58% ipsi-contra; Figures 1F and 1G). In addition, aNs are homogeneously distributed along the dorsoventral axis of the spinal cord (44%–56% ventral-dorsal), while dNs are mostly found in the ventral aspect (86%–13% ventral-dorsal; Figures 1F and 1G). Given the importance of positional organization in the spinal cord as a determinant of neuronal specification, connectivity, and function,[21–24] these distinctions suggest the existence of subtypes with different functions in sensory processing and motor control.

Identification of long ascending neurons belonging to the V3 and V0g families

We next sought to identify labeled neurons based on their molecular identity and performed single-nucleus transcriptome analysis. We used RVΔG H2B-mCherry to label aNs and dNs and dissociated mCherry$^+$ nuclei from the lumbar and cervical spinal cord (Figure 2A). We isolated 960 nuclei (480 aNs and 480 dNs) via fluorescence-activated nucleus sorting and prepared sequencing libraries using the CEL-Seq2 protocol.[25] 616 nuclei passed standard quality control criteria (Figures S3A–S3C), and bioinformatics analysis grouped them into six clusters (Figure 2B). We assigned ascending and descending identities based on the spinal level of origin of the nuclei and confirmed that the expression of the caudal spinal cord marker *Hoxc10* was selectively enriched in nuclei originating from the lumbar segment (Figures 2C and 2D). Surprisingly, aNs and dNs did not exhibit spatial segregation (Figures 2B–2D). Next, we assessed expression levels of local (*Neurod2*) and projection (*Zfhx3*) neuron markers.[26] As expected, we observed selective enrichment of *Zfhx3* in our dataset (Figures S3D–S3F). Expression of Zfhx3 at the protein level was confirmed in retrogradely labeled aNs and dNs (Figures S3G and S3H), validating this gene as a general marker of aNs and dNs. Moreover, we also confirmed Hoxc10 protein expression in aNs (Figure S3I). Differential gene expression analysis showed that clusters 4 and 5 were enriched in canonical markers of two cardinal classes of spinal interneurons (Figure 2E).[27] Cluster 4 was characterized by genes defining the Pitx2$^+$ subset of V0 interneurons (*Pitx2*, *Crhbp*, and *Cartpt*), and cluster 5 by markers of the V3 family (*Sim1* and *Nkx6-1*).[28] By contrast, we failed to identify known markers for the remaining clusters. Thus, transcriptome analysis assigned V0 and V3 identities to two propriospinal neuron clusters.

Next, we sought to validate the results of our bioinformatic analysis *in vivo*. The lumbar origin of nuclei in clusters 4 and 5 indicated an ascending phenotype for both populations (Figures 2C and 2D). We genetically labeled V3 neurons by taking advantage of *Sim1^{Cre}* mice.[29] Following unilateral injection of G-deleted rabies virus encoding for nuclear localized GFP (RVΔG H2B-GFP) in the cervical spinal cord of *Sim1^{Cre}; Rosa$^{lsl\text{-}tdTomato}$* (Ai14) mice,[30] we found that ~20% of the ascending population (GFP$^+$) were V3 neurons labeled by tdTomato (Figures S4A–S4C). These neurons were predominantly located in the dorsal contralateral spinal cord and accounted for 15% of the V3 population at lumbar level (Figure S4D). These results validated our transcriptome analysis and aligned with recent findings identifying a subset of lumbar V3 interneurons projecting to the cervical spinal cord.[13] We then characterized cluster 4 neurons. To label putative Pitx2$^+$ aNs, we bilaterally injected a retro adeno-associated virus (AAV) expressing GFP in a Cre-dependent manner (retro AAV FLEX-GFP) into the cervical spinal cord of *Pitx2^{Cre}; Rosa$^{lsl\text{-}tdTomato}$* mice (Figure 3A).[31] Analysis of lumbar levels revealed tdTomato$^+$; GFP$^+$ neurons located around the central canal, consistent with the stereotyped position of Pitx2$^+$ V0 neurons[15] and representing about 15% of the total population (Figures 3B–3D). Pitx2$^+$ V0 neurons comprise cholinergic (V0c) and glutamatergic (V0g) subsets.[15] Absence of choline acetyltransferase (*Chat*) expression in cluster 4 nuclei and in retrogradely labeled Pitx2$^+$ aNs indicated a glutamatergic phenotype (Figures S4E–S4G). Indeed, colocalization of *Pitx2* with *Slc17a6* in aNs confirmed V0g identity (Figures 3E–3G). Finally, we tested whether a population of descending V0g neurons exists by assessing *Pitx2* and *Slc17a6* expression in dNs, but we did not observe any rabies-labeled Pitx2$^+$ neurons at cervical levels (Figures 3H–3J). These results confirm the existence of long aNs belonging to the V3 family[13] and identify a subset of glutamatergic Pitx2$^+$ V0g neurons with ascending projections to the cervical spinal cord (V0g-aNs).

V0g-aNs are integrated in spinal sensorimotor circuits

We focused on V0g-aNs that represent a novel subset of both aNs and V0 neurons. We examined their input connectivity using rabies monosynaptic tracing.[32] In order to selectively target V0g-aNs, we crossed *Pitx2^{Cre}* mice with a reporter line expressing rabies G protein, TVA receptor, and nuclear GFP following Cre- and Flp-dependent recombination (*Rosa^{dsHTB}*).[33] Injection of

Please cite this article in press as: Toscano et al., A spinal circuit for skilled locomotion, Current Biology (2025), https://doi.org/10.1016/j.cub.2025.09.030

CellPress
OPEN ACCESS

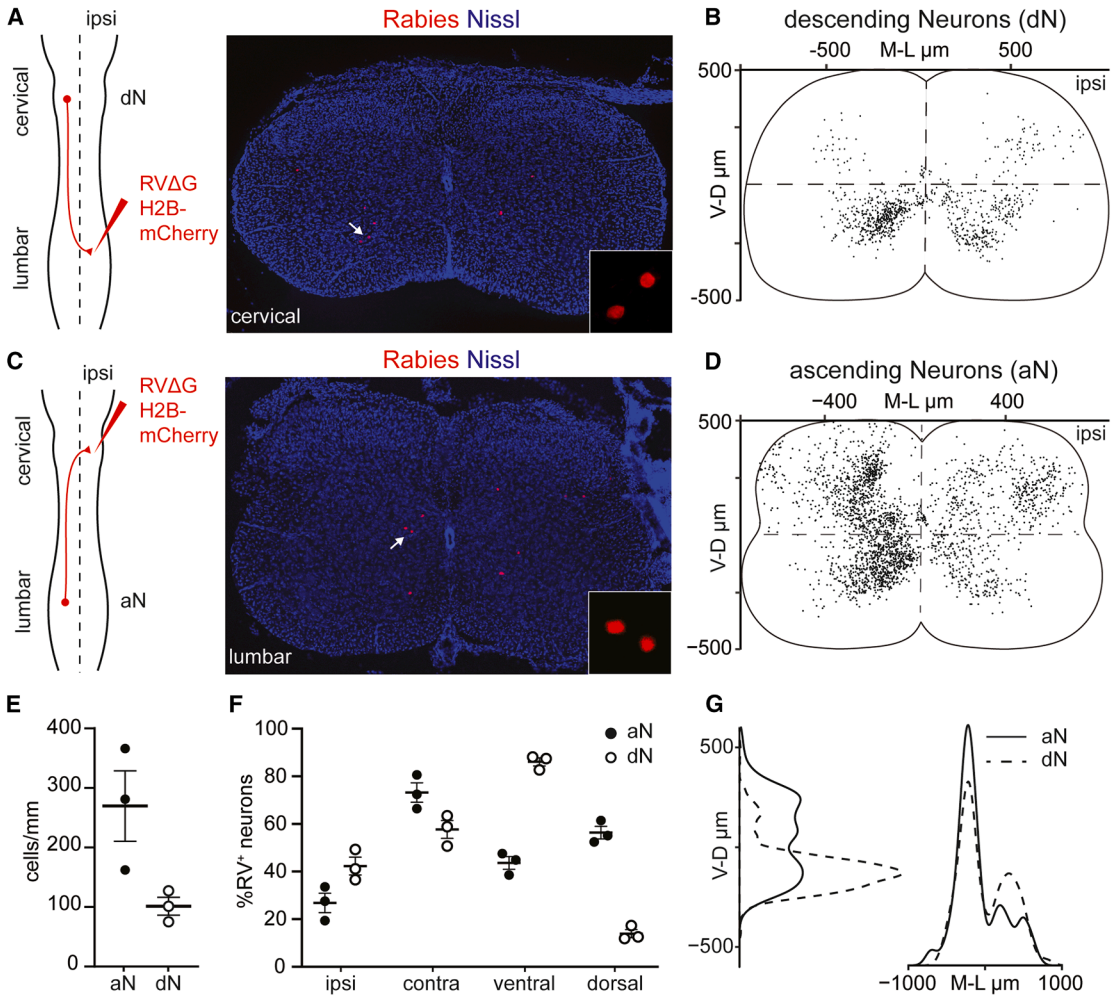

Figure 1. Anatomical characterization of long ascending and descending neurons

(A) Rabies injection strategy (unilateral, L3-L4) and representative image of infected dNs (mCherry$^+$) in the cervical spinal cord of P5–P8 C57BL6/J mice. Inset: magnification of nuclei indicated by the arrow.

(B) Position of dNs in the cervical spinal cord along the mediolateral and dorsoventral axes (n = 3 mice). Each dot represents one neuron.

(C) Rabies injection strategy (unilateral, C6-C7) and representative image of infected aNs (mCherry$^+$) in the lumbar spinal cord of P5–P8 C57BL6/J mice. Inset: magnification of nuclei indicated by the arrow.

(D) Position of aNs in the lumbar spinal cord along the mediolateral and dorsoventral axes (n = 3 mice). Each dot represents one neuron.

(E) Number of aNs and dNs labeled (n = 3 mice; mean ± SEM).

(F) Percentage of labeled aNs and dNs in the ipsilateral, contralateral, dorsal, and ventral spinal cord (mean ± SEM).

(G) Dorsoventral and mediolateral distribution of aNs and dNs (n = 3 mice).

See also Figures S1 and S2 and Table S1.

retro AAV Flp into the cervical spinal cord of *Pitx2^{Cre}; Rosa^{dsHTB}* mice resulted in specific targeting of V0g-aNs as indicated by GFP labeling (Figures 4A and 4B). Subsequent intraspinal injection of RVΔG-mCherry/EnvA at lumbar levels caused selective primary infection of V0g-aNs (starter neurons: rabies$^+$; GFP$^+$) and reproducible monosynaptic spread to presynaptic neurons (rabies$^+$; GFP$^-$; Figures 4A–4C and S5A–S5C). Starter cells showed the characteristic positioning of Pitx2$^+$ V0 neurons around the central canal (Figures 4B and S5B). We found presynaptic neurons mainly at lumbar levels and mostly localized in the intermediate spinal cord, with sparse labeling in the dorsal horn and few neurons residing in ventral areas (Figures 4B and S5A). Notably, we did not detect any labeling in dorsal root ganglia, indicating that V0g-aNs do not receive direct input from somatosensory neurons. However, we found presynaptic neurons residing in lamina X, within or near the neuroepithelium, and extending a characteristic bud into the central canal (Figure 4D). These are anatomical and morphological signatures of CSF-cNs,[16] intraspinal sensory neurons that have been implicated in skilled locomotion in mice.[17,18] In order to further validate this finding, we genetically labeled the presynaptic boutons of CSF-cNs (*Pkd2l1^{Cre}; Rosa$^{lsl\text{-}Synaptophysin\text{-}tdTomato}$*; Figure 4E)[34] and visualized aNs via cervical injection of RVΔG GFP. In these animals, we observed tdTomato$^+$ puncta juxtaposed to GFP$^+$;

Please cite this article in press as: Toscano et al., A spinal circuit for skilled locomotion, Current Biology (2025), https://doi.org/10.1016/j.cub.2025.09.030

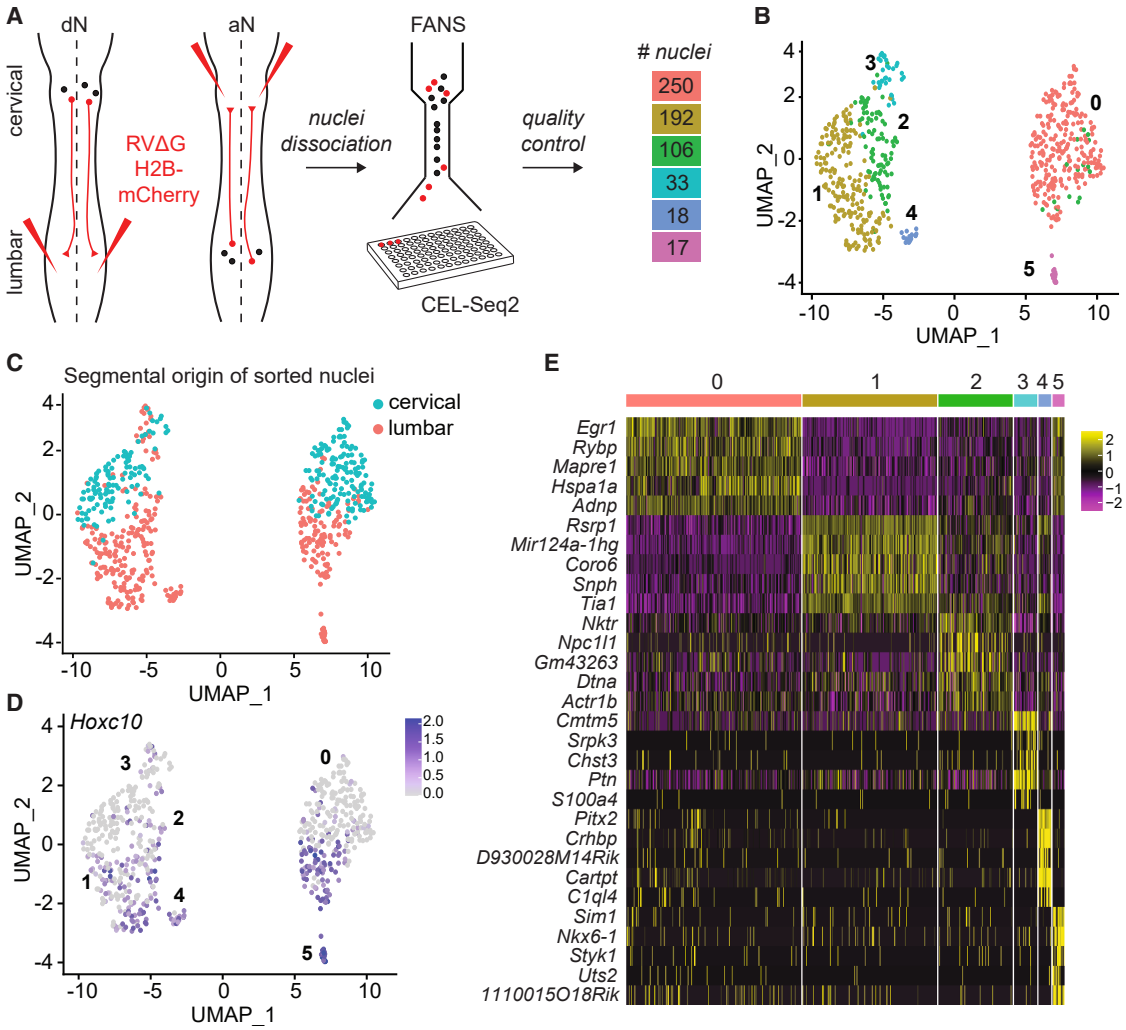

Figure 2. Single-nucleus RNA sequencing of long ascending and descending neurons

(A) Schematic representation of the experimental workflow for obtaining, sequencing, and analyzing aNs and dNs. Mice received a bilateral injection of RVΔG H2B-mCherry at either the C6-C7 or L3-L4 levels to label aNs and dNs, respectively. Following dissection of C1-T1 or L1-L6 spinal segments, mCherry$^+$ nuclei were sorted into ten 96-well plates (5 plates for each population). Sequencing libraries were prepared following the CEL-Seq2 protocol and processed using next-generation sequencing. Quality check control considering unique molecular identifier (UMI) counts excluded 344 nuclei out of 960. Clustering analysis assigned 616 nuclei to 6 clusters. The number of nuclei in each cluster is reported.

(B) Uniform manifold approximation and projection (UMAP) visualization of the neuron clusters.

(C) UMAP visualization of neuron clusters color-coded according to the cervical (teal) and lumbar (salmon) origin of the nuclei. Cervical-residing neurons correspond to dNs, and lumbar-residing neurons to aNs.

(D) UMAP visualization of the expression level of the lumbar spinal cord marker *Hoxc10*. Scale bar, log-normalized expression.

(E) Differential gene expression analysis. Each gene in a cluster is compared with its distribution across the remaining clusters. Positive values indicate upregulation, and negative values indicate downregulation. The genes displayed represent the most differentially expressed genes per cluster ranked according to the adjusted *p* value (*p*val_adj) (see STAR Methods). Scale bar, log-fold change (logFC).

See also Figure S3.

Pitx2$^+$ aNs (Figure 4F), thus confirming that CSF-cNs are a source of presynaptic input to V0g-aNs.

Next, we characterized V0g-aNs output connectivity by selective labeling of V0g-aNs axons and presynaptic boutons. We injected a retro AAV expressing Flp recombinase in a Cre-dependent manner (retro AAV DIO-Flpo) in the cervical spinal cord and an AAV driving Flp-dependent expression of membrane-bound GFP (mGFP) and synaptically tagged Ruby (sRuby) at lumbar levels of *Pitx2^{Cre}* mice (AAV FLExFRT-mGFP-sRuby; Figure 4G). Successful targeting of V0g-aNs was confirmed by labeling of neurons in lumbar lamina X (Figure 4H). In addition, we observed mGFP$^+$ axons and sRuby$^+$ presynaptic boutons in the intermediate spinal cord around the central canal and in the ventral horn with several instances of synaptic puncta juxtaposed to the cell bodies of ChAT$^+$ V0c and motor neurons (Figure 4H). At cervical levels, we similarly observed V0g-aNs axons mostly confined to the intermediate and ventral spinal cord making synaptic contacts with V0c

Please cite this article in press as: Toscano et al., A spinal circuit for skilled locomotion, Current Biology (2025), https://doi.org/10.1016/j.cub.2025.09.030

CellPress
OPEN ACCESS

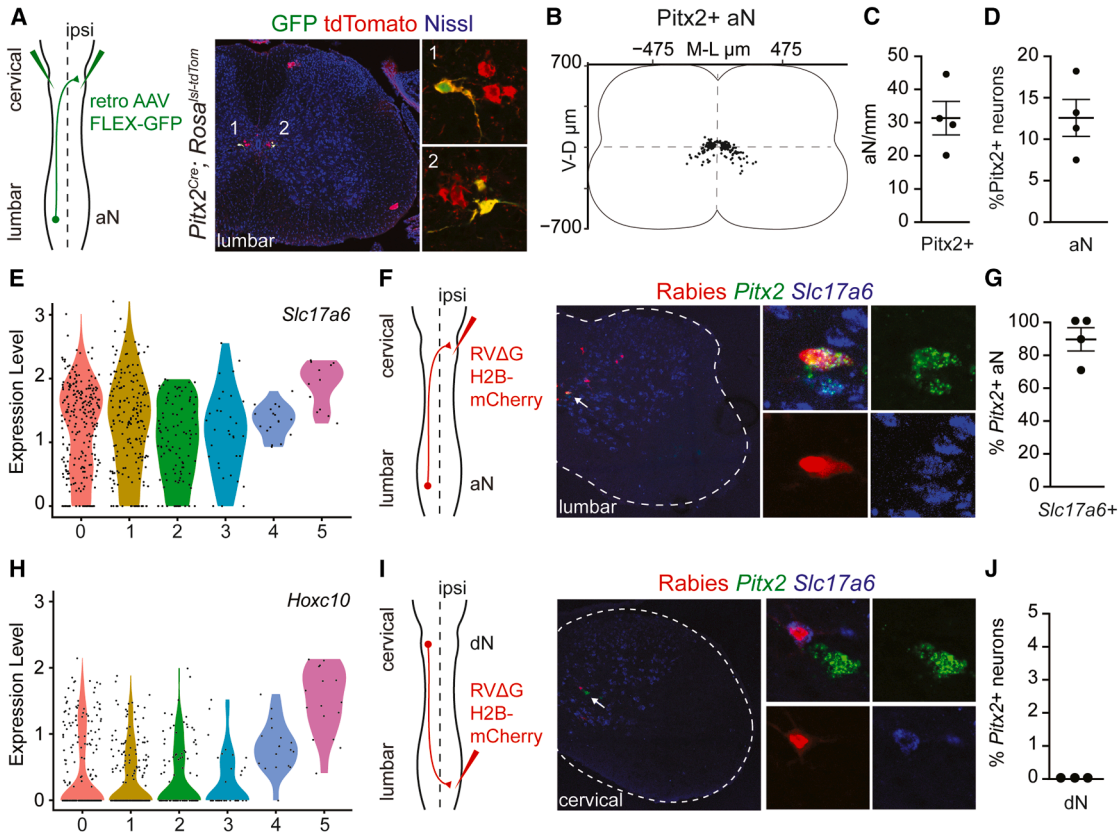

Figure 3. Characterization of Pitx2$^+$ ascending neurons

(A) Schematic (left) illustrating the bilateral retro AAV FLEX-GFP injection (C6-C7) used to retrogradely label Pitx2$^+$ aNs and representative images (right) of Pitx2$^+$ aNs (GFP$^+$; tdTomato$^+$) in the lumbar spinal cord of *Pitx2^{Cre}; Rosa$^{lsl\text{-}tdTom}$* mice.

(B) Reconstruction of Pitx2$^+$ aNs position in the lumbar spinal cord (n = 4 mice).

(C) Number of labeled Pitx2$^+$ aNs per mm in the lumbar spinal cord (n = 4 mice, mean ± SEM).

(D) Percentage of Pitx2$^+$ neurons belonging to the aNs population (n = 4 mice, mean ± SEM).

(E) Violin plot showing expression levels of the glutamatergic marker *Slc17a6* (logcounts).

(F) Schematic (left) illustrating the unilateral RVΔG H2B-mCherry injection at C6-C7 used for labeling aNs and representative images (right) of rabies-labeled aNs (mCherry$^+$) and mRNA expression of *Pitx2* and *Slc17a6*.

(G) Percentage of Pitx2$^+$ aNs expressing *Slc17a6* (n = 4 mice, mean ± SEM).

(H) Violin plot showing expression levels of the lumbar spinal cord marker *Hoxc10* (logcounts).

(I) Schematic (left) illustrating unilateral RVΔG H2B-mCherry injection (C6-C7) used for labeling dNs and representative images (right) of a cervical spinal cord showing rabies-labeled dNs (mCherry$^+$) and mRNA expression of *Pitx2* and *Slc17a6*.

(J) Percentage of dNs expressing *Pitx2* (n = 3 mice, mean ± SEM).

See also Figure S4.

and motor neurons (Figure 4I). At supraspinal level, we only found sparse labeling in the medulla around the central canal (Figure 4J). Altogether, the data indicate that V0g-aNs receive sensory information at lumbar level and distribute it, locally and at cervical level, to premotor and motor neurons, with limited supraspinal connectivity to the brainstem.

V0g-aNs are dispensable for open-field and treadmill locomotion

To investigate the role of V0g-aNs in locomotor control, we devised a strategy to acutely eliminate this population. We injected retro AAV Flpo in the cervical spinal cord of triple transgenic *Pitx2^{Cre}; Rosa$^{lsl\text{-}fsf\text{-}tdTomato}$; Mapt$^{lsl\text{-}fsf\text{-}DTR}$* mice (Ai65; *Rosa^{dstdTomato}; Mapt^{dsDTR}*)[35,36] to drive expression of tdTomato and diphtheria toxin receptor (DTR) in V0g-aNs (Figures 5A and 5B). After 4 weeks, we performed behavioral tests to determine baseline motor performance (“pre”; Figure 5C). We then injected diphtheria toxin (DT) (or PBS as a control) at lumbar level to selectively eliminate V0g-aNs. In order to estimate aNs targeting efficiency, we co-injected, along with PBS or DT, AAV fDIO-YFP to drive Flp-dependent YFP expression in aNs infected by cervical retro AAV Flp injection (Figures 5B–5D). Finally, we repeated the behavioral tests 2 weeks after PBS or DT injection. Post hoc histological analysis confirmed elimination of V0g-aNs in DT-injected mice (Figure 5E). In addition, we assessed the number of YFP$^+$ neurons, representing aNs (Pitx2$^-$) that are not susceptible to DT-mediated ablation, and found no significant difference in their number between conditions. Thus, the ratio of

Please cite this article in press as: Toscano et al., A spinal circuit for skilled locomotion, Current Biology (2025), https://doi.org/10.1016/j.cub.2025.09.030

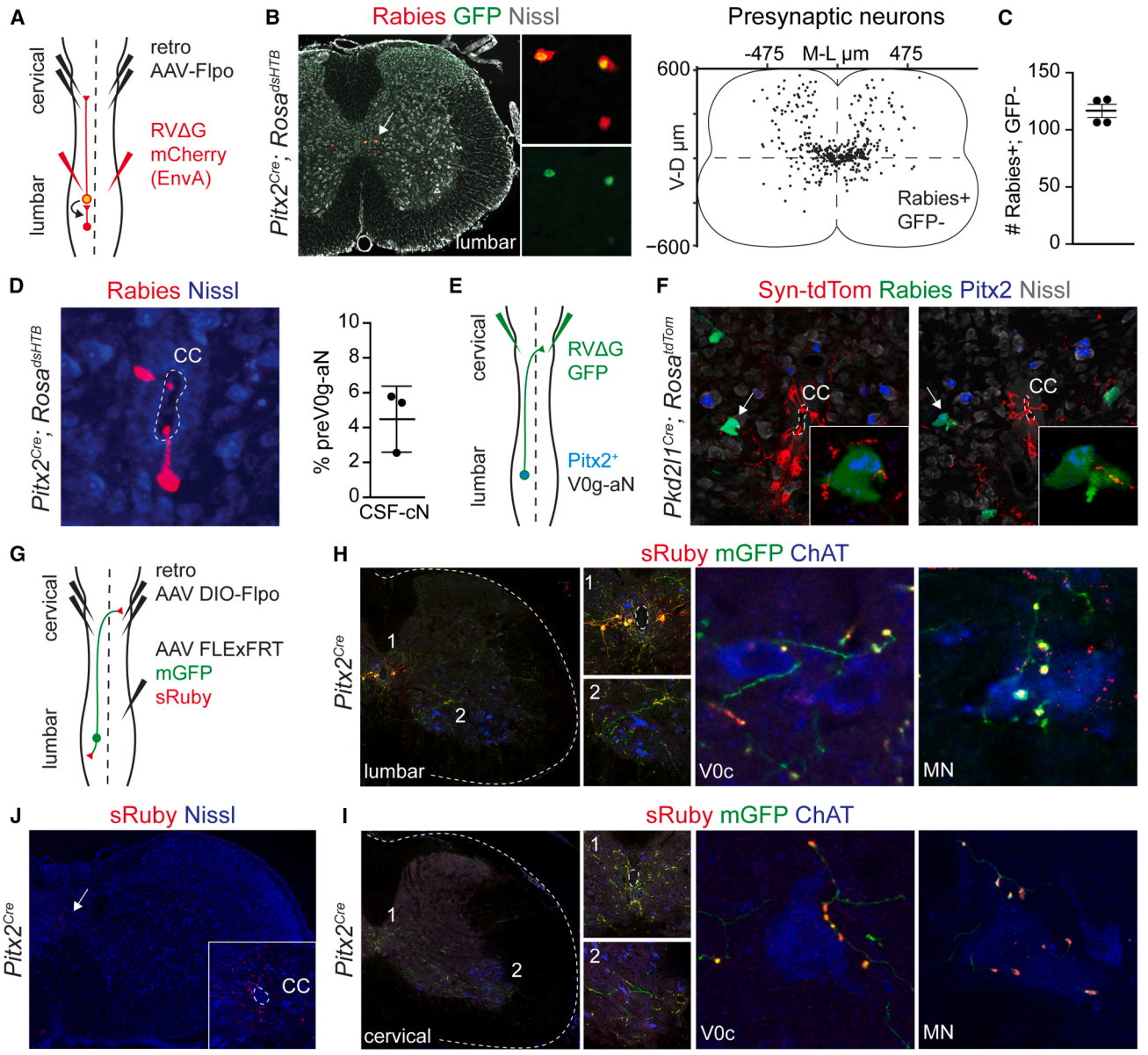

Figure 4. Input and output connectivity of V0g-aNs

(A) Schematic illustrating the bilateral retro AAV Flpo injection (C5-C6 and C6-C7) followed by bilateral RVΔG mCherry/EnvA (L1-L2) used for labeling V0g-aNs presynaptic neurons.

(B) Representative images (left) of V0g-aNs starter (Rabies^{+}; GFP^{+}) and presynaptic neurons (Rabies^{+}; GFP^{-}) in the lumbar spinal cord of a *Pitx2^{Cre}; Rosa^{dsHTB}* and reconstruction (right) of presynaptic neurons (Rabies^{+}; GFP^{-}) position.

(C) Total number of presynaptic neurons (Rabies^{+}; GFP^{+}; n = 4 mice, mean ± SEM).

(D) Representative image (left) and quantification (right) of V0g-aNs presynaptic neurons (Rabies^{+}; GFP^{-}) residing within or around neuroepithelium in lamina X of the spinal cord and extending a bud in the central canal (n = 3 mice, mean ± SEM).

(E) Schematic illustrating bilateral RVΔG GFP injection at C6-C7 used for retrograde labeling of Pitx2^{+} V0g-aNs in the spinal cord of *Pkd2l1^{Cre}*; *Rosa$^{lsl\text{-}Synaptophysin\text{-}tdTomato}$* mice.

(F) Representative images of CSF-cNs synaptic boutons (Syn-tdTomato^{+}) juxtaposed to V0g-aNs (GFP^{+}; Pitx2^{+}) in the lumbar spinal cord of *Pkd2l1^{Cre}*; *Rosa$^{lsl\text{-}Synaptophysin\text{-}tdTomato}$* mice (insets show magnifications of neurons marked by the arrows).

(G) Schematic illustrating the bilateral retro AAV DIO-Flpo injection (C5-C6 and C6-C7) followed by unilateral AAV FLExFRT-mGFP-2A-synaptophysin-mRuby (L1-L2) used for labeling of V0g-aNs axons (membrane GFP: mGFP) and presynaptic puncta (synaptophysin-mRuby: sRuby) in *Pitx2^{Cre}* mice.

(H) Representative images showing labeling of V0g-aNs axons and presynaptic boutons at the lumbar level (left) and high magnifications of presynaptic puncta on V0c (middle) and motor neurons (right).

(legend continued on next page)

Please cite this article in press as: Toscano et al., A spinal circuit for skilled locomotion, Current Biology (2025), https://doi.org/10.1016/j.cub.2025.09.030

CellPress
OPEN ACCESS

V0g-aNs over the aNs population was significantly reduced after DT injection (Figures 5F and 5G).

In order to study the effect of elimination of V0g-aNs on locomotion, we first evaluated volitional motor activity using the open-field test. We did not observe any differences in distance traveled, speed, percentage of time spent moving, and number of rears between PBS- and DT-treated mice, indicating that elimination of V0g-aNs does not result in gross disruptions in motor control (Figures 5H–5K). Next, to quantitatively study locomotion, we performed high-resolution whole-body kinematic analysis at the treadmill. We tested speeds ranging from 0.2 to 0.8 m/s to assess different gaits from walking (typically observed at 0.2–0.3 m/s) to trot (0.3–0.7 m/s) and gallop (at 0.8 m/s).[2] By using markerless body part tracking,[37] we extracted 100 kinematic parameters to provide a comprehensive quantification of locomotor features (Table S2). Principal-component analysis revealed no effect of DT or PBS treatments but precisely clustered animals according to speed, indicating that elimination of V0g-aNs did not affect kinematics (Figure 5L; Video S1). We further analyzed key metrics describing locomotion, such as cadence, stance duration, and swing duration, and found no significant difference between PBS and DT treatments at all speeds tested (Figures S6A–S6C). Altogether, these results indicate that V0g-aNs are dispensable for open-field and treadmill locomotion.

V0g-aNs are necessary for skilled locomotion

Long ascending neurons have been shown to contribute to the coordination of limb movements in a task- and context-dependent manner,[12] indicating that these circuits might be differentially recruited depending on the involvement of supraspinal control and sensory information. Thus, we evaluated the effect of eliminating V0g-aNs on more challenging tasks that require dynamic adaptation of basic rhythmic patterns of limb movements.[38,39] First, we used ladder walking to assess skilled paw placement and fine motor control. We observed a significant increase in the number of paw placement mistakes in DT-injected mice (Figure 6A; Video S2). Interestingly, we only observed significant differences in hindlimb performance (Figure 6B). Next, we tested beam walking, which also emphasizes balance and whole-body coordination. We used a round (1 cm diameter) and a square (0.5 cm wide) elevated beam. We found an increase in the number of paw placement mistakes after elimination of V0g-aNs in both settings (Figures 6C and 6E; Videos S3 and S4). As on the horizontal ladder, the deficit was specific to the hindlimbs on the square beam, whereas forelimbs were also significantly affected on the round beam (Figures 6D and 6F). Finally, we tested whether differences in grip and/or tactile sensation arising from elimination of V0g-aNs could contribute to the phenotype, but we did not find any significant differences between PBS and DT-injected animals in grip strength, cotton swab, and von Frey tests (Figures S5D–S5F). Together, these results show that V0g-aNs, while dispensable for walking and running, are selectively required for skilled locomotion.

DISCUSSION

In this study, we combined viral tracing, transcriptomic, and behavioral analyses to identify and functionally characterize a novel subtype of lumbar ascending neurons belonging to the glutamatergic subset of the Pitx2$^+$ V0 family. Our analysis indicates that V0g-aNs are integrated into sensorimotor circuits and receive input from CSF-cNs—intraspinal sensory neurons that monitor body axis movement[16]—previously shown to contribute to adaptive motor control in mice.[17,18] Functionally, V0g-aNs, while dispensable for on-ground locomotion, are necessary for the execution of skilled locomotor movements.

We took advantage of rabies tracing to anatomically and molecularly characterize long ascending and descending neurons that reciprocally connect the cervical and lumbar enlargements. Single-nucleus transcriptome analysis identified two populations of aNs belonging to the V3 (Sim1$^+$) and V0 (Pitx2$^+$) classes of spinal neurons.[27] Unfortunately, experimental limitations, including the low number of neurons analyzed, glial contamination, and expression of stress response genes, precluded identification of more clusters. We validated and anatomically characterized V3-aNs, confirming results recently reported by another group,[13] and decided to focus our efforts on Pitx2$^+$ aNs that represent a novel subtype of both propriospinal and V0 neurons. These neurons constitute at least 10%–15% of the Pitx2$^+$ V0 population, are exclusively glutamatergic, and do not include a descending population. While the function of V0 neurons has been extensively studied, the role of V0g neurons, and in particular of an ascending subset, has not been investigated yet. Elimination of all V0 neurons results in synchronization of forelimb and hindlimb movements at all speeds, indicating a central role in regulating left-right alternation.[5,7] The V0 family comprises inhibitory (V0d, *Pax*$^+$) and excitatory (V0v, *Evx1/2*$^+$, and *Vglut2*$^+$) subtypes.[5] Elimination of glutamatergic V0v neurons does not affect walk and bound gaits at low and high speeds, respectively, but causes selective loss of the fast-paced alternating trot.[2] Our data show that V0g-aNs, which represent a small subset of V0v neurons,[15] do not affect locomotion at a wide range of speeds (0.2–0.8 m/s) requiring different gaits (from walk to gallop). Instead, we found a specific role in adapting movements to the more challenging requirements of skilled locomotion. In contrast to our findings, a previous study did not report defects at the ladder and beam tests upon acute silencing of aNs.[12] This apparent discrepancy may reflect differences in animal models (mouse vs. rat), targeting specificity (V0g-aNs vs. all aNs), and manipulation (ablation vs. silencing).

Perturbation of spinal circuits gating mechanosensory information impairs performance in skilled locomotor tasks such as ladder and beam walking.[40] Indeed, the role of cutaneous sensory feedback in regulating corrective reflexes and balance has been demonstrated in humans, cats, and mice.[41–46] Dorsal spinal circuits have been proposed to recruit downstream excitatory neurons within the locomotor CPG to tailor motor responses to the specific requirements of the task.[33,44] Moreover,

(I) Representative images showing labeling of V0g-aNs axons and presynaptic boutons at cervical level (left) and high magnifications of presynaptic puncta on a V0c (middle) and motor neurons (right).
(J) Representative images showing labeling of V0g-aNs presynaptic boutons in the medulla (inset shows magnification of the CC area).
CC, central canal; MN, motor neuron.
See also Figure S5.

Please cite this article in press as: Toscano et al., A spinal circuit for skilled locomotion, Current Biology (2025), https://doi.org/10.1016/j.cub.2025.09.030

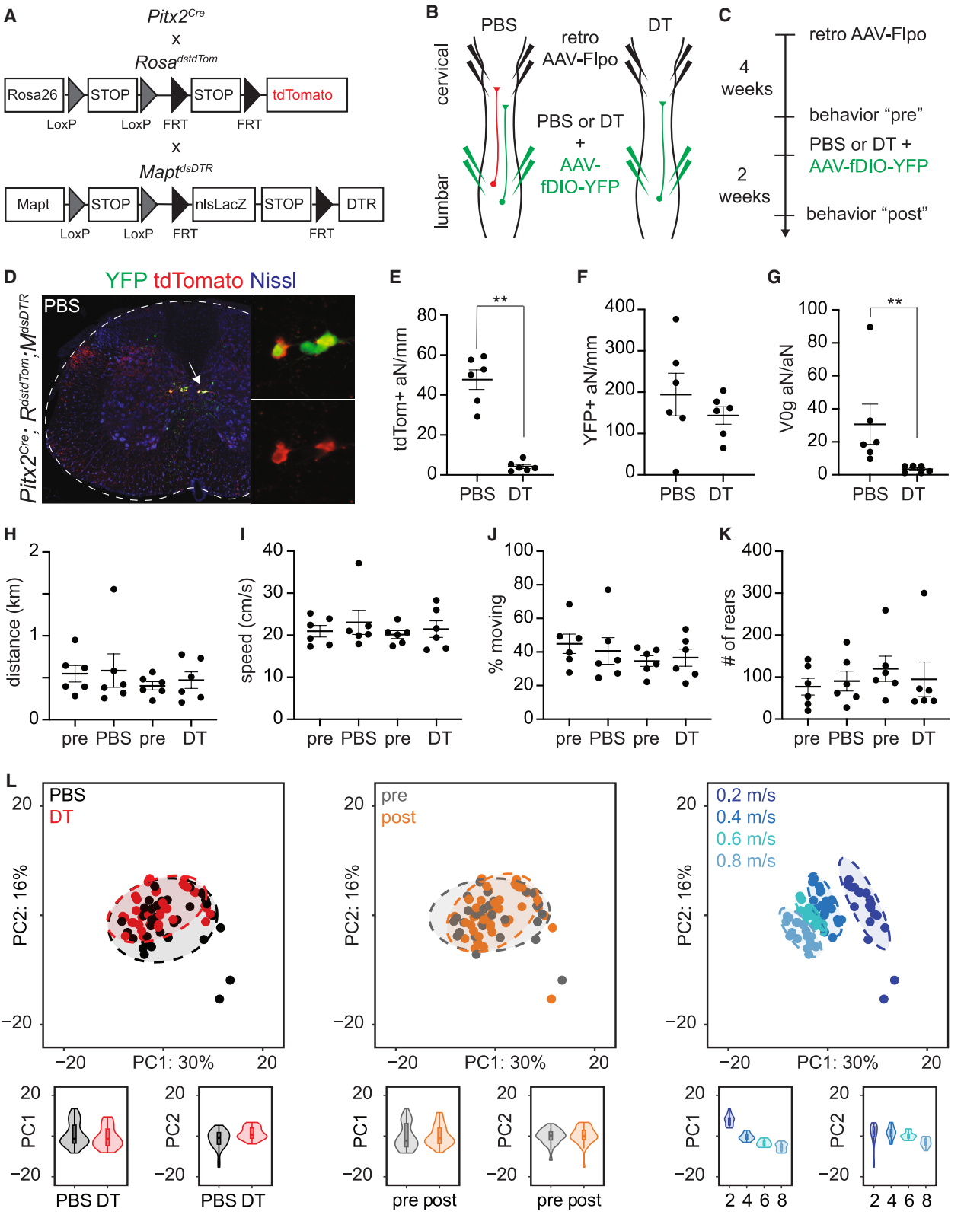

(legend on next page)

Please cite this article in press as: Toscano et al., A spinal circuit for skilled locomotion, Current Biology (2025), https://doi.org/10.1016/j.cub.2025.09.030

CellPress
OPEN ACCESS

proprioceptive information has been shown to be critical for controlling the precision of hindlimb foot placement during locomotion.[47] While our monosynaptic rabies experiments indicate that V0g-aNs do not receive direct somatosensory input, we observed presynaptic neurons in the dorsal and intermediate spinal cord that could indirectly convey tactile and proprioceptive information. In addition, we found direct input from CSF-cNs, intraspinal chemo- and mechanosensory neurons that survey CSF composition and flow.[16] In lamprey and zebrafish, CSF-cNs relay information about spinal bending to control swimming and posture.[48–50] In mice, elimination of CSF-cNs does not affect general motor activity or the generation of locomotor patterns but results in specific defects at ladder and beam walking, thus phenocopying the effect of eliminating V0g-aNs.[17,18] In this context, our data suggest that V0g-aNs act downstream of CSF-cNs to integrate an additional source of sensory information that is used to adapt motor programs controlled by the CPG to the requirements of more complex locomotor tasks. Interestingly, anatomical studies in zebrafish and mice indicate that CSF-cNs are part of an evolutionarily conserved spinal circuit, including V0 interneurons, that modulate motor neuron activity.[17,49,51] In line with these observations, V0g-aNs send synaptic output to V0c and motor neurons at both lumbar and cervical levels. Although V0g-aNs long-distance connections directly impinge on forelimb motor circuits, the observed functional defects are more pronounced at the level of the hindlimbs. It is possible that sensory information provided by V0g-aNs can be partially or completely compensated at forelimb level by other sources, such as the visual and vibrissal systems. More in general, these data indicate that the ascending output of V0g-aNs does not have a classic propriospinal role in controlling interlimb coordination but instead may serve to relay a copy of sensory information from the lumbar to the cervical spinal cord to adjust motor output.

Altogether, this study identifies a novel spinal neuron subtype and characterizes it at anatomical and functional levels to show that V0g-aNs represent a key component of spinal sensorimotor circuits dedicated to the execution of skilled locomotor movements. The data pave the way for future work aimed at understanding how spinal circuits that govern different aspects of movement, such as basic and skilled locomotion, are organized and interact to precisely adjust locomotor patterns in response to environmental complexity.

RESOURCE AVAILABILITY

Lead contact

Further information and requests should be directed to the lead contact, Niccolò Zampieri (niccolo.zampieri@mdc-berlin.de).

Materials availability

All unique reagents generated in this study are available from the lead contact.

Data and code availability

- Single-nucleus RNA sequencing data have been deposited at GEO, accession number: GSE304439.
- This paper does not report original code.
- All additional information required to reanalyze the data reported in this paper is available from the lead contact upon request.

ACKNOWLEDGMENTS

The authors thank the Advanced Light Microscopy, Genomics, and Animal Phenotyping platforms at the MDC. We thank Liana Kosizki for technical support and Sampurna Chakrabarti and Mohammed Khallaf for assistance with the cotton swab and von Frey assays. We are grateful to Julien Bouvier, Graziana Gatto, Amanda Pocratsky, and members of the laboratory for critically reading the manuscript. C.B. is supported by the Deutsche Forschungsgemeinschaft under Germany's Excellence Strategy (EXC-2049 – 39068808). C.B. and N.Z. are supported by the Helmholtz Association.

AUTHOR CONTRIBUTIONS

Conceptualization, E.T. and N.Z.; investigation, E.T., M.G., N.E., P.T., and E.D.L.; formal analysis, E.T., N.E., A.S., A.M., and N.Z.; writing – original draft, E.T. and N.Z.; writing – review and editing, E.T., N.E., M.G., A.S., E.D.L., C.B., and N.Z.; and supervision, N.Z.

DECLARATION OF INTERESTS

The authors declare no competing interests.

STAR★METHODS

Detailed methods are provided in the online version of this paper and include the following:

- KEY RESOURCES TABLE
- EXPERIMENTAL MODEL AND STUDY PARTICIPANT DETAILS
  - Mice
- METHOD DETAILS
  - Perfusion and tissue preparation
  - Immunohistochemistry
  - Fluorescent *in situ* hybridization

Figure 5. Elimination of V0g-aNs does not perturb kinematic parameters during treadmill locomotion

(A) *Pitx2*^{Cre}; *Rosa*^{dstdTom}; *Mapt*^{dsDTR} triple transgenic mice used in neuronal ablation experiments of V0g-aNs.

(B) Schematic illustrating the bilateral retro AAV Flpo injection (C5-C6 and C6-C7) used to drive expression of tdTomato and DTR in V0g-aNs and the bilateral injection (L2-L3 and L3-L4) of PBS or DT—along with AAV fDIO-YFP to label all aNs—to ablate V0g-aNs.

(C) Experimental timeline of "pre" and "post" behavioral experiments in relation to PBS or DT injections.

(D) Representative image of a lumbar spinal cord showing YFP and tdTomato expression in a *Pitx2*^{Cre}; *Rosa*^{dstdTom}; *Mapt*^{dsDTR} control (PBS) mouse (scale bar, 100 μm) and high magnifications of representative tdTomato$^+$, YFP$^+$ V0g-aNs.

(E) Number of tdTomato$^+$ aNs in PBS- and DT-treated animals (n = 6 mice per group, mean ± SEM; unpaired Mann-Whitney test, $^{**}p$ = 0.0022).

(F) Number of YFP$^+$ aNs in PBS- and DT-treated animals (n = 6 mice per group, mean ± SEM; unpaired Mann-Whitney test, $p > 0.05$).

(G) Percentage of V0g-aNs among the total aNs population in PBS- and DT-treated animals (n = 6 mice per group, mean ± SEM; unpaired Mann-Whitney test, $^{**}p$ = 0.0022).

(H–K) Total distance, speed, percentage of time spent moving, and number of rears during the open-field test before (pre) and after PBS and DT treatments (mean ± SEM, linear mixed model analysis; all $p > 0.05$).

(L) Principal-component analysis of kinematic parameters. Colors indicate PBS (black) and DT (red) treatment; pre (gray) and post (orange) treatment; and speed, 0.2 (blue), 0.4 (dodger blue), 0.6 (cyan), and 0.8 (sky blue) m/s.

See also Figure S6 and Table S2 and Video S1.

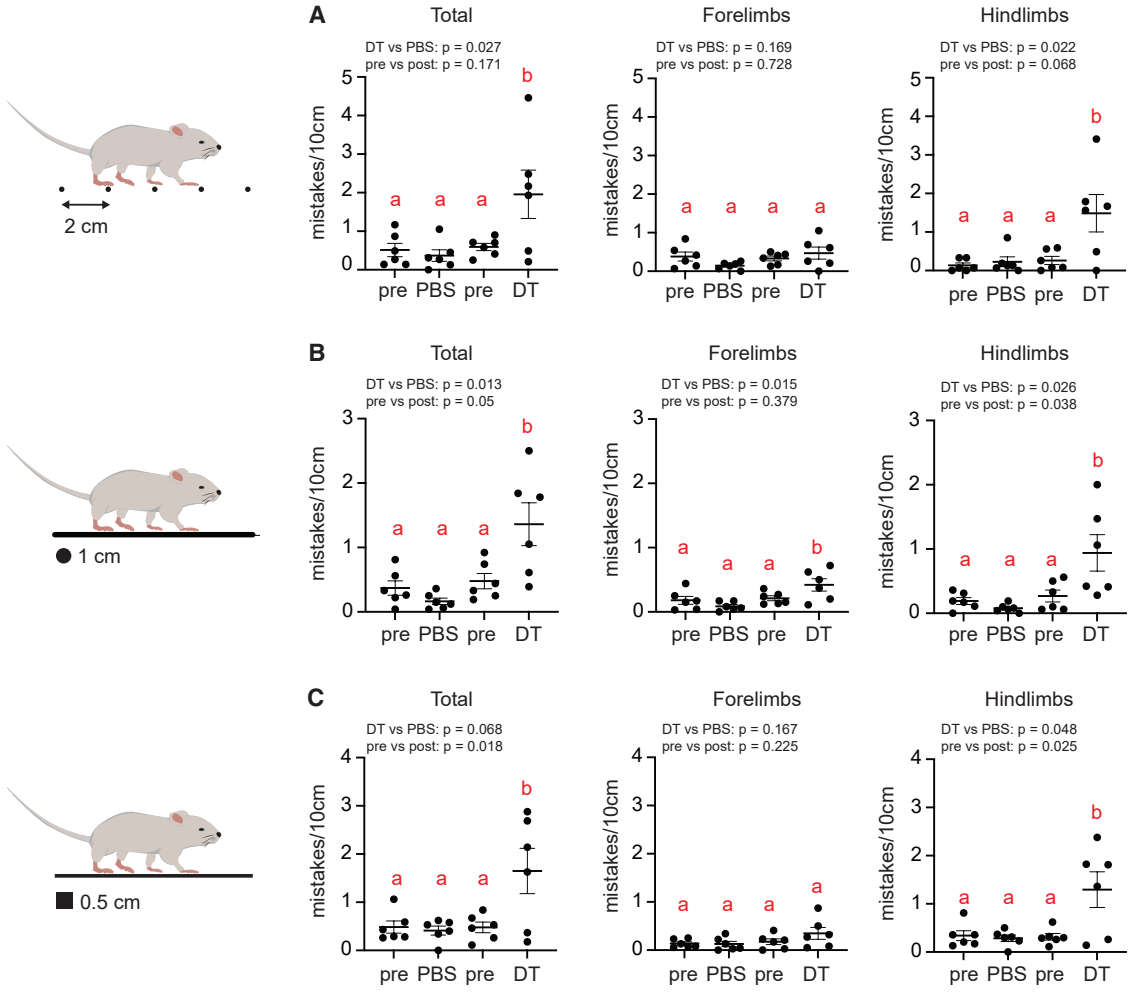

Figure 6. Elimination of V0g-aNs affects skilled locomotion

(A) Quantification of total (left), forelimb (center), and hindlimb (right) paw placement mistakes per 10 cm at the horizontal ladder (rungs 2 cm apart) before and after PBS or DT treatment.

(B) Quantification of total (left), forelimb (center), and hindlimb (right) paw placement mistakes per 10 cm at the round beam (1 cm diameter) before and after PBS or DT treatment.

(C) Quantification of total (left), forelimb (center), and hindlimb (right) paw placement mistakes per 10 cm at the square beam (0.5 cm wide) before and after PBS or DT treatment.

For each group, $n = 6$ mice. Data are mean ± SEM. The letters summarize the results of post hoc pairwise comparisons. Pairs that do not display the same letter are significantly different.

See also Figure S5 and Videos S2, S3, and S4.

SUPPLEMENTAL INFORMATION

Supplemental information can be found online at https://doi.org/10.1016/j.cub.2025.09.030.

Received: February 5, 2025
Revised: August 7, 2025
Accepted: September 8, 2025

REFERENCES

1. Grillner, S., and El Manira, A. (2020). Current principles of motor control, with special reference to vertebrate locomotion. Physiol. Rev. *100*, 271–320. https://doi.org/10.1152/physrev.00015.2019.

2. Bellardita, C., and Kiehn, O. (2015). Phenotypic characterization of speed-associated gait changes in mice reveals modular organization of

Please cite this article in press as: Toscano et al., A spinal circuit for skilled locomotion, Current Biology (2025), https://doi.org/10.1016/j.cub.2025.09.030

locomotor networks. Curr. Biol. *25*, 1426–1436. https://doi.org/10.1016/j.cub.2015.04.005.

3. Rybak, I.A., Dougherty, K.J., and Shevtsova, N.A. (2015). Organization of the Mammalian Locomotor CPG: Review of Computational Model and Circuit Architectures Based on Genetically Identified Spinal Interneurons (1,2,3). eNeuro *2*, ENEURO.0069-15.2015. https://doi.org/10.1523/ENEURO.0069-15.2015.
4. Rossignol, S., Dubuc, R., and Gossard, J.-P. (2006). Dynamic Sensorimotor Interactions in Locomotion. Physiol. Rev. *86*, 89–154. https://doi.org/10.1152/physrev.00028.2005.
5. Talpalar, A.E., Bouvier, J., Borgius, L., Fortin, G., Pierani, A., and Kiehn, O. (2013). Dual-mode operation of neuronal networks involved in left-right alternation. Nature *500*, 85–88. https://doi.org/10.1038/nature12286.
6. Crone, S.A., Quinlan, K.A., Zagoraiou, L., Droho, S., Restrepo, C.E., Lundfald, L., Endo, T., Setlak, J., Jessell, T.M., Kiehn, O., et al. (2008). Genetic Ablation of V2a Ipsilateral Interneurons Disrupts Left-Right Locomotor Coordination in Mammalian Spinal Cord. Neuron *60*, 70–83. https://doi.org/10.1016/j.neuron.2008.08.009.
7. Lanuza, G.M., Gosgnach, S., Pierani, A., Jessell, T.M., and Goulding, M. (2004). Genetic Identification of Spinal Interneurons that Coordinate Left-Right Locomotor Activity Necessary for Walking Movements. Neuron *42*, 375–386. https://doi.org/10.1016/S0896-6273(04)00249-1.
8. Crone, S.A., Zhong, G., Harris-Warrick, R., and Sharma, K. (2009). In mice lacking V2a Interneurons, Gait Depends on Speed of Locomotion. J. Neurosci. *29*, 7098–7109. https://doi.org/10.1523/JNEUROSCI.1206-09.2009.
9. Sherrington, C.S., and Laslett, E.E. (1903). Observations on some spinal reflexes and the interconnection of spinal segments. J. Physiol. *29*, 58–96. https://doi.org/10.1113/jphysiol.1903.sp000946.
10. Flynn, J.R., Graham, B.A., Galea, M.P., and Callister, R.J. (2011). The role of propriospinal interneurons in recovery from spinal cord injury. Neuropharmacology *60*, 809–822. https://doi.org/10.1016/j.neuropharm.2011.01.016.
11. Ruder, L., Takeoka, A., and Arber, S. (2016). Long-Distance Descending Spinal Neurons Ensure Quadrupedal Locomotor Stability. Neuron *92*, 1063–1078. https://doi.org/10.1016/j.neuron.2016.10.032.
12. Pocratsky, A.M., Shepard, C.T., Morehouse, J.R., Burke, D.A., Riegler, A. S., Hardin, J.T., Beare, J.E., Hainline, C., States, G.J., Brown, B.L., et al. (2020). Long ascending propriospinal neurons provide flexible, context-specific control of interlimb coordination. eLife *9*, e53565. https://doi.org/10.7554/eLife.53565.
13. Zhang, H., Shevtsova, N.A., Deska-Gauthier, D., Mackay, C., Dougherty, K.J., Danner, S.M., Zhang, Y., and Rybak, I.A. (2022). The role of V3 neurons in speed-dependent interlimb coordination during locomotion in mice. eLife *11*, e73424. https://doi.org/10.7554/eLife.73424.
14. Flynn, J.R., Conn, V.L., Boyle, K.A., Hughes, D.I., Watanabe, M., Velasquez, T., Goulding, M.D., Callister, R.J., and Graham, B.A. (2017). Anatomical and Molecular Properties of Long Descending Propriospinal Neurons in Mice. Front. Neuroanat. *11*, 5. https://doi.org/10.3389/fnana.2017.00005.
15. Zagoraiou, L., Akay, T., Martin, J.F., Brownstone, R.M., Jessell, T.M., Miles, G.B., Thomas, M., and Miles, G.B. (2009). A Cluster of Cholinergic Premotor Interneurons Modulates Mouse Locomotor Activity. Neuron *64*, 645–662. https://doi.org/10.1016/j.neuron.2009.10.017.
16. Wyart, C., Carbo-Tano, M., Cantaut-Belarif, Y., Orts-Del'Immagine, A., and Böhm, U.L. (2023). Cerebrospinal fluid-contacting neurons: multimodal cells with diverse roles in the CNS. Nat. Rev. Neurosci. *24*, 540–556. https://doi.org/10.1038/s41583-023-00723-8.
17. Gerstmann, K., Jurčić, N., Blasco, E., Kunz, S., de Almeida Sassi, F., Wanaverbecq, N., and Zampieri, N. (2022). The role of intraspinal sensory neurons in the control of quadrupedal locomotion. Curr. Biol. *32*, 2442–2453.e4. https://doi.org/10.1016/j.cub.2022.04.019.
18. Nakamura, Y., Kurabe, M., Matsumoto, M., Sato, T., Miyashita, S., Hoshina, K., Kamiya, Y., Tainaka, K., Matsuzawa, H., Ohno, N., et al. (2023). Cerebrospinal fluid-contacting neuron tracing reveals structural and functional connectivity for locomotion in the mouse spinal cord. eLife *12*, e83108. https://doi.org/10.7554/eLife.83108.
19. Wickersham, I.R., Finke, S., Conzelmann, K.K., and Callaway, E.M. (2007). Retrograde neuronal tracing with a deletion-mutant rabies virus. Nat. Methods *4*, 47–49. https://doi.org/10.1038/nmeth999.
20. Ballion, B., Morin, D., and Viala, D. (2001). Forelimb locomotor generators and quadrupedal locomotion in the neonatal rat. Eur. J. Neurosci. *14*, 1727–1738. https://doi.org/10.1046/j.0953-816x.2001.01794.x.
21. Tripodi, M., and Arber, S. (2012). Regulation of motor circuit assembly by spatial and temporal mechanisms. Curr. Opin. Neurobiol. *22*, 615–623. https://doi.org/10.1016/j.conb.2012.02.011.
22. Balaskas, N., Ng, D., and Zampieri, N. (2020). The Positional Logic of Sensory-Motor Reflex Circuit Assembly. Neuroscience *450*, 142–150. https://doi.org/10.1016/j.neuroscience.2020.04.038.
23. Osseward, P.J., and Pfaff, S.L. (2019). Cell type and circuit modules in the spinal cord. Curr. Opin. Neurobiol. *56*, 175–184. https://doi.org/10.1016/j.conb.2019.03.003.
24. Ronzano, R., Skarlatou, S., Barriga, B.K., Bannatyne, B.A., Bhumbra, G. S., Foster, J.D., Moore, J.D., Lancelin, C., Pocratsky, A.M., Özyurt, M. G., et al. (2022). Spinal premotor interneurons controlling antagonistic muscles are spatially intermingled. eLife *11*, e81976. https://doi.org/10.7554/eLife.81976.
25. Hashimshony, T., Senderovich, N., Avital, G., Klochendler, A., de Leeuw, Y., Anavy, L., Gennert, D., Li, S., Livak, K.J., Rozenblatt-Rosen, O., et al. (2016). CEL-Seq2: sensitive highly-multiplexed single-cell RNA-Seq. Genome Biol. *17*, 77. https://doi.org/10.1186/s13059-016-0938-8.
26. Osseward, P.J., Amin, N.D., Moore, J.D., Temple, B.A., Barriga, B.K., Bachmann, L.C., Beltran, F., Gullo, M., Clark, R.C., Driscoll, S.P., et al. (2021). Conserved genetic signatures parcellate cardinal spinal neuron classes into local and projection subsets. Science *372*, 385–393. https://doi.org/10.1126/science.abe0690.
27. Bikoff, J.B. (2019). Interneuron diversity and function in the spinal motor system. Curr. Opin. Physiol. *8*, 36–43. https://doi.org/10.1016/j.cophys.2018.12.013.
28. Russ, D.E., Cross, R.B.P., Li, L., Koch, S.C., Matson, K.J.E., Yadav, A., Alkaslasi, M.R., Lee, D.I., Le Pichon, C.E., Menon, V., et al. (2021). A harmonized atlas of mouse spinal cord cell types and their spatial organization. Nat. Commun. *12*, 5722. https://doi.org/10.1038/s41467-021-25125-1.
29. Zhang, Y., Narayan, S., Geiman, E., Lanuza, G.M., Velasquez, T., Shanks, B., Akay, T., Dyck, J., Pearson, K., Gosgnach, S., et al. (2008). V3 Spinal Neurons Establish a Robust and Balanced Locomotor Rhythm during Walking. Neuron *60*, 84–96. https://doi.org/10.1016/j.neuron.2008.09.027.
30. Madisen, L., Zwingman, T.A., Sunkin, S.M., Oh, S.W., Zariwala, H.A., Gu, H., Ng, L.L., Palmiter, R.D., Hawrylycz, M.J., Jones, A.R., et al. (2010). A robust and high-throughput Cre reporting and characterization system for the whole mouse brain. Nat. Neurosci. *13*, 133–140. https://doi.org/10.1038/nn.2467.
31. Liu, W., Selever, J., Lu, M.-F., and Martin, J.F. (2003). Genetic dissection of Pitx2 in craniofacial development uncovers new functions in branchial arch morphogenesis, late aspects of tooth morphogenesis and cell migration. Development *130*, 6375–6385. https://doi.org/10.1242/dev.00849.
32. Wickersham, I.R., Lyon, D.C., Barnard, R.J.O.O., Mori, T., Finke, S., Conzelmann, K.-K.K., Young, J.A.T.T., and Callaway, E.M. (2007). Monosynaptic restriction of transsynaptic tracing from single, genetically targeted neurons. Neuron *53*, 639–647. https://doi.org/10.1016/j.neuron.2007.01.033.
33. Bourane, S., Grossmann, K.S., Britz, O., Dalet, A., Del Barrio, M.G., Stam, F.J., Garcia-Campmany, L., Koch, S., and Goulding, M. (2015). Identification of a Spinal Circuit for Light Touch and Fine Motor Control. Cell *160*, 503–515. https://doi.org/10.1016/j.cell.2015.01.011.

Please cite this article in press as: Toscano et al., A spinal circuit for skilled locomotion, Current Biology (2025), https://doi.org/10.1016/j.cub.2025.09.030

34. Ye, W., Chang, R.B., Bushman, J.D., Tu, Y.-H., Mulhall, E.M., Wilson, C.E., Cooper, A.J., Chick, W.S., Hill-Eubanks, D.C., Nelson, M.T., et al. (2016). The K^+ channel K_{IR} 2.1 functions in tandem with proton influx to mediate sour taste transduction. Proc. Natl. Acad. Sci. USA *113*, E229–E238. https://doi.org/10.1073/pnas.1514282112.

35. Madisen, L., Garner, A.R., Shimaoka, D., Chuong, A.S., Klapoetke, N.C., Li, L., van der Bourg, A., Niino, Y., Egolf, L., Monetti, C., et al. (2015). Transgenic mice for intersectional targeting of neural sensors and effectors with high specificity and performance. Neuron *85*, 942–958. https://doi.org/10.1016/j.neuron.2015.02.022.

36. Britz, O., Zhang, J., Grossmann, K.S., Dyck, J., Kim, J.C., Dymecki, S., Gosgnach, S., and Goulding, M. (2015). A genetically defined asymmetry underlies the inhibitory control of flexor–extensor locomotor movements. eLife *4*, e04718. https://doi.org/10.7554/eLife.04718.

37. Mathis, A., Mamidanna, P., Cury, K.M., Abe, T., Murthy, V.N., Mathis, M. W., and Bethge, M. (2018). DeepLabCut: markerless pose estimation of user-defined body parts with deep learning. Nat. Neurosci. *21*, 1281–1289. https://doi.org/10.1038/s41593-018-0209-y.

38. Rossignol, S. (1996). Neural Control of Stereotypic Limb Mouvement. In Handbook of Physiology Section 12 (Wiley), pp. 173–216.

39. Lundberg, A., and Phillips, C.G. (1973). T. Graham Brown's film on locomotion in the decerebrate cat. J. Physiol. *231*, 90P–91P.

40. Gatto, G., Bourane, S., Ren, X., Di Costanzo, S., Fenton, P.K., Halder, P., Seal, R.P., and Goulding, M.D. (2021). A Functional Topographic Map for Spinal Sensorimotor Reflexes. Neuron *109*, 91–104.e5. https://doi.org/10.1016/j.neuron.2020.10.003.

41. Perry, S.D., McIlroy, W.E., and Maki, B.E. (2000). The role of plantar cutaneous mechanoreceptors in the control of compensatory stepping reactions evoked by unpredictable, multi-directional perturbation. Brain Res. *877*, 401–406. https://doi.org/10.1016/S0006-8993(00)02712-8.

42. Bouyer, L.J.G., and Rossignol, S. (2003). Contribution of Cutaneous Inputs from the Hindpaw to the Control of Locomotion. I. Intact Cats. J. Neurophysiol. *90*, 3625–3639. https://doi.org/10.1152/jn.00496.2003.

43. Panek, I., Bui, T., Wright, A.T.B., and Brownstone, R.M. (2014). Cutaneous afferent regulation of motor function. Acta Neurobiol. Exp. (Wars.) *74*, 158–171. https://doi.org/10.55782/ane-2014-1982.

44. Paixão, S., Loschek, L., Gaitanos, L., Alcalà Morales, P., Goulding, M., and Klein, R. (2019). Identification of Spinal Neurons Contributing to the Dorsal Column Projection Mediating Fine Touch and Corrective Motor Movements. Neuron *104*, 749–764.e6. https://doi.org/10.1016/j.neuron.2019.08.029.

45. Rossignol, S., Dubuc, J., and Gossard, J.-P. (2006). Dynamic Sensorimotor Interactions in Locomotion. Physiol. Rev. *86*, 89–154. https://doi.org/10.1152/physrev.00028.2005.-Locomotion.

46. Koch, S.C., Del Barrio, M.G., Dalet, A., Gatto, G., Günther, T., Zhang, J., Seidler, B., Saur, D., Schüle, R., and Goulding, M. (2017). RORβ Spinal Interneurons Gate Sensory Transmission during Locomotion to Secure a Fluid Walking Gait. Neuron *96*, 1419–1431.e5. https://doi.org/10.1016/j.neuron.2017.11.011.

47. Mayer, W.P., and Akay, T. (2021). The role of muscle spindle feedback in the guidance of hindlimb movement by the ipsilateral forelimb during locomotion in mice. eNeuro *8*, ENEURO.0432-21.2021. https://doi.org/10.1523/ENEURO.0432-21.2021.

48. Böhm, U.L., Prendergast, A., Djenoune, L., Nunes Figueiredo, S.N., Gomez, J., Stokes, C., Kaiser, S., Suster, M., Kawakami, K., Charpentier, M., et al. (2016). CSF-contacting neurons regulate locomotion by relaying mechanical stimuli to spinal circuits. Nat. Commun. *7*, 10866. https://doi.org/10.1038/ncomms10866.

49. Hubbard, J.M., Böhm, U.L., Prendergast, A., Tseng, P.B., Newman, M., Stokes, C., and Wyart, C. (2016). Intraspinal Sensory Neurons Provide Powerful Inhibition to Motor Circuits Ensuring Postural Control during Locomotion. Curr. Biol. *26*, 2841–2853. https://doi.org/10.1016/j.cub.2016.08.026.

50. Jalalvand, E., Robertson, B., Wallén, P., and Grillner, S. (2016). Ciliated neurons lining the central canal sense both fluid movement and pH through ASIC3. Nat. Commun. *7*, 10002. https://doi.org/10.1038/ncomms10002.

51. Fidelin, K., Djenoune, L., Stokes, C., Prendergast, A., Gomez, J., Baradel, A., Del Bene, F., and Wyart, C. (2015). State-dependent modulation of locomotion by GABAergic spinal sensory neurons. Curr. Biol. *25*, 3035–3047. https://doi.org/10.1016/j.cub.2015.09.070.

52. Skarlatou, S., Hérent, C., Toscano, E., Mendes, C.S., Bouvier, J., and Zampieri, N. (2020). Afadin Signaling at the Spinal Neuroepithelium Regulates Central Canal Formation and Gait Selection. Cell Rep. *31*, 107741. https://doi.org/10.1016/j.celrep.2020.107741.

53. Santuz, A., Ekizos, A., Eckardt, N., Kibele, A., and Arampatzis, A. (2018). Challenging human locomotion: stability and modular organisation in unsteady conditions. Sci. Rep. *8*, 2740. https://doi.org/10.1038/s41598-018-21018-4.

54. Insafutdinov, E., Pishchulin, L., Andres, B., Andriluka, M., and Schiele, B. (2016). DeeperCut: A Deeper, Stronger, and Faster Multi-person Pose Estimation Model. Preprint at arXiv. https://doi.org/10.1007/978-3-319-46466-4_3.

55. He, K., Zhang, X., Ren, S., and Sun, J. (2016). Deep Residual Learning for Image Recognition. In IEEE Conference on Computer Vision and Pattern Recognition (CVPR) (IEEE), pp. 770–778. https://doi.org/10.1109/CVPR.2016.90.

56. Santuz, A., Laflamme, O.D., and Akay, T. (2022). The brain integrates proprioceptive information to ensure robust locomotion. J. Physiol. *600*, 5267–5294. https://doi.org/10.1113/JP283181.

57. Maiwald, C., Sterzing, T., Mayer, T.A., and Milani, T.L. (2009). Detecting foot-to-ground contact from kinematic data in running. Footwear Sci. *1*, 111–118. https://doi.org/10.1080/19424280903133938.

58. Chaplan, S.R., Bach, F.W., Pogrel, J.W., Chung, J.M., and Yaksh, T.L. (1994). Quantitative assessment of tactile allodynia in the rat paw. J. Neurosci. Methods *53*, 55–63. https://doi.org/10.1016/0165-0270(94)90144-9.

59. Piepho, H.-P. (2004). An Algorithm for a Letter-Based Representation of All-Pairwise Comparisons. J. Comp. Graph. Stat. *13*, 456–466. https://doi.org/10.1198/1061860043515.

Please cite this article in press as: Toscano et al., A spinal circuit for skilled locomotion, Current Biology (2025), https://doi.org/10.1016/j.cub.2025.09.030

CellPress
OPEN ACCESS

STAR★METHODS

KEY RESOURCES TABLE

REAGENT or RESOURCE	SOURCE	IDENTIFIER
Antibodies		
Sheep anti-Zfhx3	R&D systems	AF7384; RRID: AB_11127859
Rabbit anti-Hoxc10	Atlas Antibodies	HPA053919; RRID: AB_2682308
Goat anti-Chat	Millipore	AB144P; RRID: AB_2079751
Rabbit anti-dsRed	Takara	632496; RRID: AB_10013483
Rabbit anti-RFP	Rockland	600-401-379; RRID: AB_2209751
Chicken anti-GFP	Abcam	AB13970; RRID: AB_300798
Rabbit anti-Pitx2	Columbia University	CU1533, RRID: AB_3697299
Alexa-488 anti-sheep	Jackson ImmunoResearch	RRID: AB_2340744
Alexa-488 anti-chicken	Jackson ImmunoResearch	RRID: AB_2337390
Alexa-488 anti-rabbit	Jackson ImmunoResearch	RRID: AB_2338046
Cy5 anti-goat	Jackson ImmunoResearch	RRID: AB_2340415
Cy3 anti-rabbit	Jackson ImmunoResearch	RRID: AB_2307443
RNAscope probes		
Mm- Pitx2	ACDBio	412841 – C1
Mm- Slc17a6 (Vglut2)	ACDBio	319171 – C3
Mm- Slc32a1 (Vgat)	ACDBio	319191 – C2
Bacterial and Virus Strains		
RV SADB19 ΔG H2B-mCherry	Produced in house	N/A
RV SADB19 ΔG H2B-GFP	Produced in house	N/A
RV SADB19 ΔG GFP	Produced in house	N/A
RV SADB19 ΔG H2B-mCherry/EnvA	Viral Core Facility (Charité, University Berlin)	N/A
AAV2/2 retro hSyn-Flpo	Viral Core Facility (Charité, University Berlin)	Addgene #60663
AAV2/2 retro CAG flex GFP	Viral Core Facility (Charité, University Berlin)	Addgene #28304
AAV2/2 retro EF1a-fDIO FLPo	Viral Core Facility (Charité, University Berlin)	Addgene #87306
AAV2/9 hSyn FLExFRT-mGFP-2A-synaptophysin-mRuby	Viral Core Facility (Charité, University Berlin)	Addgene #71761
AAV2/9 Ef1a-fDIO EYFP	Viral Core Facility (Charité, University Berlin	Addgene #55641
Chemicals		
Diphtheria toxin (DT)	Sigma Aldrich	D0564
NeuroTrace 435/455	Thermo Fisher	N21479
NeuroTrace 640/660	Thermo Fisher	N21483
Vectashield	VectorLabs	H-1000
RNAscope Multiplex Fluorescent Kit v2	ACDBio	323100
Tissue-Tek O.C.T. compound	Sakura	4583
Experimental Models: Organisms/Strains		
C57BL/6J	Jackson Laboratory	RRID: IMSR_JAX:000664
Pitx2::Cre	Liu et al.[31]	RRID: MGI:2445429
Pkd2l1::Cre	Ye et al.[34]	RRID: MGI:6451758
Sim1::Cre	Zhang et al.[29]	RRID: MGI: 3839912
Rosa::lsl-tdTomato (Ai14)	Madisen et al.[30]	RRID: IMSR_JAX:007914
Rosa::dsHTB	Bourane et al.[33]	RRID: MGI:5518925
Mapt::dsDTR	Britz et al.[36]	RRID: MGI:5911677
Rosa::lsl-fsf-tdTomato (Ai65)	Madisen et al.[35]	RRID: IMSR_JAX:021875

(*Continued on next page*)

Continued

REAGENT or RESOURCE	SOURCE	IDENTIFIER
Rosa::lsl-Synaptophysin-tdTomato (Ai34)	Jackson Laboratory	RRID: IMSR_JAX:012570
Software and Algorithms		
R	R Project for Statistical Computing	RRID: SCR_001905
Deeplabcut	Mathis et al.[37]	RRID: SCR_021391
Imaris	Oxford Instruments	RRID: SCR_007370
GraphPad Prism	SciCrunch Registry	RRID: SCR_002798

EXPERIMENTAL MODEL AND STUDY PARTICIPANT DETAILS

Mice

All animal procedures were performed in accordance with European Research Council Directives and were approved by the Regional Office for Health and Social Affairs Berlin (LAGeSo) under license numbers G122/15 and G0093/20. Mice were bred and maintained under standard conditions on a 12 hours light/dark cycle with access to food and water *ad libitum*. Both male and female mice (from postnatal to adult stages) were used in our experiments.

METHOD DETAILS

Perfusion and tissue preparation

Mice were anesthetized by intraperitoneal injection of Ketamine (120 mg/kg) and Xylazine (10 mg/kg) and transcardially perfused with ice-cold PBS, followed by 4% PFA in 0.1 M phosphate buffer. Ventral laminectomy was performed to expose the spinal cord and tissue was fixed overnight with 4% PFA at 4°C. The next day, the spinal cord was washed with ice-cold PBS and incubated in 30% sucrose for 1 day at 4°C for cryoprotection. Samples were embedded in Tissue-Tek O.C.T. compound (Sakura).

Immunohistochemistry

For immunohistochemistry, the embedded spinal cord tissue was sectioned with a Leica cryostat. Subsequently, the slides were incubated twice for 10 minutes with 0.1 % Triton X-100 in PBS (0.1 % PBX) for permeabilization. Followed by incubation with a solution containing primary antibodies diluted in 0.1% PBX at 4°C overnight. The next day, slides were washed three times for 5 minutes with 0.1% PBX followed by incubation with a solution containing secondary antibodies and NeuroTrace (Thermo Fisher) diluted in 0.1% PBX for 1h at room temperature. Finally, slides were washed three times with 0.1 % PBX and mounted with Vectashield (VectorLabs) antifade mounting medium. Images were acquired using a Zeiss LSM800 confocal microscope.

Fluorescent *in situ* hybridization

For fluorescent in situ hybridization, embedded spinal cord blocks were sectioned at a thickness of 20 μm. The RNAscope Multiplex Fluorescent Kit v2 (ACDBio) was used for the hybridization process. Tissue sections were air-dried, fixed with 4% PFA in PBS (ice-cold) for 15 minutes, and dehydrated using a series of ethanol washes (50%, 70%, and 100% for 5 minutes each). Afterward, the sections were treated with a hydrogen peroxide solution at room temperature for 15 minutes to inhibit endogenous peroxidase activity, followed by another wash in 100% ethanol for 5 minutes. Protease IV was applied at room temperature for 30 minutes. After three PBS washes, probes were applied, and hybridization occurred in a humidified oven at 40°C for 2 hours. Amplification was performed using Amp1, Amp2, and Amp3, each for 30 minutes at 40°C. For detection, each section was treated with channel-specific HRP (HRP-C1, HRP-C2, HRP-C3) for 15 minutes, followed by TSA-mediated fluorophore binding for 30 minutes, and HRP blocking for 15 minutes (all steps at 40°C). Images were acquired using a Zeiss LSM800 confocal microscope.

Retrograde tracing experiments

For retrograde tracing experiments we used RVΔG H2B-mCherry (SAD B19; 3 x 10^{11} VP/ml), RVΔG H2B-GFP (SAD B19; 2.24 x 10^{11} VP/ml) and retro AAV2/2 FLEX-GFP (6.69 x 10^{11} VG/ml; Addgene plasmid #28304). Stereotactic spinal cord injections were performed as follows, P5-8 C57BL/6J mice were anesthetized with a mixture of 3% isoflurane and oxygen, placed under a stereotactic apparatus, and maintained using 2% isoflurane in oxygen. The injection was performed using a pulled glass capillary mounted on a 5μl Hamilton syringe filled with mineral oil. The virus was delivered in 5 x 50 nl pulses at the rate of 50 nl/s, separated by 30–60 seconds to allow the virus uptake. The cervical C6-C7 and lumbar L3-L4 levels were targeted to label aNs and dNs, respectively. The skin was closed with tissue glue (Vetbond) and the animals were left to recover from anesthesia on a warm mat and then moved back into their home cage. Animals that received RV injections were sacrificed after 3 days for histological analysis or single nucleus isolation. Mice that received AAV injections were sacrificed after 3-4 weeks for histological analysis.

Please cite this article in press as: Toscano et al., A spinal circuit for skilled locomotion, Current Biology (2025), https://doi.org/10.1016/j.cub.2025.09.030

CellPress
OPEN ACCESS

Transsynaptic tracing experiments

For transsynaptic tracing experiments, P5-P10 *Pitx2^{Cre}; Rosa$^{ds\text{-}HTB}$* mice received bilateral injection at C5-C6 and C6-C7 levels for a total of 1μl (5 x 50 nl pulses in each side and segment at a rate of 50 nl/s) of retro AAV2/2 hSynapsin-Flpo (1.34*10^{12} VG/ml; Addgene plasmid #60663). After 3 weeks, mice received a second bilateral injection at L1-L2 level (2 x 100 nl pulses in each side at a rate of 10 nl/s) of RVΔG mCherry/EnvA (SAD B19; 5*10^{8} VP/ml). Mice were sacrificed after 7 days for histological analysis.

Positional analysis

Three-dimensional positional analysis was performed as previously described.[52] Neuron quantification was performed manually in a nonblinded manner using the "Spot" function of the image analysis software IMARIS. The same function was used to obtain neuron coordinates. To account for variations in spinal cord size, orientation, and shape, the datasets were rotated and normalized against a standardized spinal cord with empirically determined dimensions. The rostrocaudal position of each neuron was tracked based on the sequential acquisition of the sections. The x, y, and z coordinates were then used to digitally map the neuron distribution. Positional datasets were processed using custom scripts in R. Contour and density plots were generated with the "ggplot2" package, which estimates the two-dimensional Gaussian density of the distribution. Correlation analysis was performed using the "corrplot" package, which calculates the similarity between experimental pairs based on the Pearson's correlation coefficient.

Synaptic boutons labeling experiments

For labeling V0g-aNs synaptic boutons, *Pitx2^{Cre}* mice received bilateral injection at C5-C6 and C6-C7 levels (5 x 50 nl pulses in each side and segment at a rate of 50 nl/s) of retro AAV2/2 EF1a-DIO-FLPo (4,02*10^{11} VG/ml; Addgene plasmid #87306). After 3 weeks, mice received a second unilateral intraspinal injection in the right L1-L2 segment with 300 nl of AAV2/9 FLExFRT-mGFP-2A-Synaptophysin-mRuby (3,45 x 10^{12} VG/ml; Addgene plasmid #71761). Mice were sacrificed after 3 weeks for histological analysis. For labeling CSF-cNs synaptic boutons on V0g-aNs, *Pkd2l1^{Cre}*; *Rosa$^{lsl\text{-}Synaptophysin\text{-}tdTomato}$* mice received bilateral injection at C6-C7 level (5 x 50 nl pulses in each side at a rate of 50 nl/s of RVΔG GFP; SAD B19, 3.23 x 10^{11} VP/ml). Mice were sacrificed after 3 days for histological analysis.

Single nucleus isolation

Mice that received lumbar or cervical bilateral injections of RVΔG H2B-mCherry (SAD B19; 3 x 10^{11} VP/ml) were sacrificed by decapitation. The cervical (C1-T1) or lumbar (L1-L6) segments were isolated to collect dNs and aNs, respectively. The spinal cord segments were cut into small pieces and placed in a Dounce homogenizer filled with ice-cold homogenization buffer. The tissue was manually homogenized with five strokes of the loose pestle, followed by 10–15 strokes of the tight pestle. Subsequently, the solution containing the dissociated nuclei was filtered through a 40 μm filter into a sorting tube and DAPI was added to a final concentration of 1 μM. Nuclei mCherry^{+}; DAPI^{+} were sorted into 96-well plates using BD FACSAria Fusion and BD FACSDiva software 8.0.1. 480 dNs were isolated from 11 animals, whereas 480 ans were sorted from 9 animals into a total of ten 96-well barcoded plates.

Library preparation and single nucleus RNA sequencing

Single-nucleus RNA libraries were prepared following the CEL-Seq2 protocol.[25] The libraries were sequenced on an Illumina NextSeq500 platform with high-output flow cells by the Next Generation Sequencing Core Facility of the Max Delbrück Center for Molecular Medicine. Data processing was done in R version 4.4.2 (R Foundation for Statistical Computing, Vienna, Austria) and Seurat v4.[53] Two thresholds were set to filter out wells without nuclei or with multiple nuclei. We set a lower threshold of 7,000 UMIs (unique molecular identifier) and an upper threshold of 50,000 UMIs per nucleus. These UMI thresholds filtered out 344 nuclei (out of 960 total), the remaining 616 nuclei (268 dNs and 348 aNs) were used for further analysis. The first 30 principal components were selected after PCA, excluding PC1 and PC4, which represented immune response and oligodendrocyte contamination. For the differential gene expression analysis, log-fold change (logFC) was computed as the logarithm (base 2) of the fold change, representing the ratio of average gene expression in a given cluster compared to the average expression across all other clusters. To assess statistical significance, a p-value was computed for each gene comparison. To correct for multiple hypothesis testing, an adjusted p-value (pval_adj) was calculated using the Bonferroni correction. The genes presented in the analysis are the five with the lowest adjusted p-values per cluster, indicating the most statistically significant differences in expression. The neighbor graph was constructed with FindNeighbors with a k parameter of 10. The clustering resolution was set to 0.4. UMAP visualization was used with the default settings.

Neuronal ablation

For the ablation experiments, P6-P8 *Pitx2^{Cre}; Rosa^{dstdTom}; Mapt^{dsDTR}* mice received bilateral injection (5 x 50 nl pulses at a rate of 50nl/s) of retro AAV2/2 hSynapsin-Flpo (1.34 x 10^{12} VG/ml; Addgene plasmid #60663) at C5-C6 and C6-C7 levels. Four weeks later, the same mice received a second intraspinal bilateral injection at L2-L3 and L3-L4 levels (200 nl of 0.4 ng/μl of DT or 200 nl of PBS diluted 1:1 with an AAV2/9 Ef1a-fDIO EYFP. 5.99 x 10^{12} VG/ml; Addgene plasmid #55641). The mice were anesthetized with a mixture of 5% isoflurane and oxygen and maintained using 2% isoflurane in oxygen. Eyes were coated in eye cream to prevent drying during anesthesia. An incision was made in the dorsal skin to expose the musculature. The musculature above and below the T13 vertebra was gently separated to expose the underlying lumbar segments. The skin was closed with absorbable sutures. Behavioral experiments were performed 10-14 days after DT/PBS injections.

Please cite this article in press as: Toscano et al., A spinal circuit for skilled locomotion, Current Biology (2025), https://doi.org/10.1016/j.cub.2025.09.030

Behavioral experiments

For locomotor tests mice were placed in the behavior room 30-60 minutes before starting the experiments, allowing them to acclimatize.

Open field test

We used the ActiMot Infrared light beam activity monitor (TSE Systems). Two light-beam frames allowed the monitoring of X, Y, and Z coordinates of the mouse. Animals were placed in the associated square acrylic glass boxes and after 10 min of habituation time, spontaneous movements were monitored for 90 min. Data were evaluated with TSE supplied software. 2

Balance beam test

To evaluate balance, we used a customized balance beam with replaceable beams of different sizes: a 90 cm-long round beam (1cm diameter) and an 80 cm-long square beam (0.5cm width). Animals were placed on one end and had to pass the beam spontaneously to reach a shelter on the other side. A mirror was placed underneath and a high-speed camera captured the passage at 30 frames/s. The two beams were assessed on the same day in the following order: first the round beam and second square beam. Analysis was blinded for the group (DT or PBS) and the day (pre or post). Mistakes were manually recorded and defined as follows: full slips of a paw off the beam and instances where the paw was not correctly placed on the top edge of the beams.

Horizontal ladder test

The horizontal ladder was customized with side walls made of acrylic glass to create a walking path and metal rungs (3 mm diameter) every 2 cm. A mirror under the horizontal ladder and the clear walls allowed tracking from the side and underneath with a high-speed camera at 30 frames/s. Animals were required to pass the walking floor spontaneously, and videos with continuous runs were analyzed. Analysis was blinded for the group (DT or PBS) and the day (pre or post). Mistakes were scored manually and defined as: a complete slip of the paw off the rung, a missed attempt to reach the rung, and when only two fingers were properly placed on the rung.

Kinematic analysis

We used a custom-made treadmill (workshop of the Zoological Institute, University of Cologne, Germany) with a transparent belt and two mirrors placed above and below the treadmill at a 45° angle. Mice were allowed to acclimate on the treadmill for about 10 minutes or until they completed a full grooming sequence. A high-speed camera captured videos at 300 frames per second. The mice were tested at speeds ranging from 0.2 to 0.8 m/s, increasing by 0.1 m/s increments, with 2–5-minute breaks between each speed. Markerless body part tracking was conducted using DeepLabCut[37] v2.3.9. We labeled 79 landmarks on 172 frames taken from 24 videos of 17 different animals assigning 95% of frames to the training set without cropping. Namely, we labeled the following landmarks. Dorsal view (top mirror): snout, head, ears, right hindlimb iliac crest and hip (highlighted by two white dots placed with an oil-based marker under brief 2.5% isoflurane anesthesia through inhalation at 1 l/min), five equidistant tail points. Sagittal view: snout, right eye, right ear, forelimb and hindlimb ankles, forelimb and hindlimb metatarsal joints, forelimb and hindlimb toe tips, right hindlimb iliac crest, right hindlimb hip, right hindlimb knee (the actual knee position was calculated in postprocessing by triangulation knowing the lengths of the femur and the tibia), five equidistant tail points, right scapula, most dorsal part of the trunk. Ventral view (bottom mirror): snout, mouth, ears, paw centers and finger tips, five equidistant tail points. We used a ResNet-50-based neural network[54,55] with default parameters for 2,300,000 training iterations and eight refinements. We validated with one shuffle and found the test error was 2.29 pixels and the train error 2.20 pixels. Each trial had a minimum duration of 1.2 seconds. Gait parameters were extracted using a custom R script: stance duration was defined as the time between touchdown and the next liftoff; swing duration as the time between liftoff and the next touchdown; and cadence as the total number of steps taken during the analyzed period. Of the 79 landmarks, we used 14 for the segmentation of the gait cycle: the twelve calibration markers, the right hindlimb metatarsal and toe tip markers. Following a procedure extensively reported previously[53,56] we processed the data to detect touchdown and lift-off of the right-side hindlimb. For touchdown estimation, we used the modified foot contact algorithm developed by Maiwald and colleagues[57] For estimating lift-off, we used the paw acceleration and jerk algorithm.[53] We found [LOe – 20 ms, LOe + 20 ms] to be the sufficiently narrow interval needed to make the initial lift-off estimation. To calculate phase values, each step cycle was normalized from 0 (beginning of stance) to 1 (end of swing). Limb coupling phase values were calculated by measuring the delay of each paw relative to the touchdown of the right hind paw (used as a reference). Phase values of 0 or 1 (± 0.25) indicated synchronization (in-phase coupling), while a value of 0.5 (± 0.25) indicated alternating movement (out-of-phase coupling).

Grip strength test

Grip strength was measured using a grip strength meter (Ugo Basile model 47200). The animals were acclimated in their home cages in the test room for 30 minutes. A trapeze bar was used to measure the strength of the forelimbs. The mouse was placed in front of the trapeze without support on its forelimbs until it grasped the trapeze. In each test, the mouse was allowed to grasp the grid and then steadily pulled by the middle of its tail until it released its grip. The strength of the hind limbs was assessed using a plastic square grid. The mouse was placed in the center of the grid, and its front limbs were placed on a separate stainless-steel grid to isolate the strength of the hindlimbs. The combined strength of the front and hind limbs was measured by placing the mouse in the center of a plastic square grid, allowing it to grasp with all limbs. Each mouse was tested five times in each test with at least one minute between trial. Between tests, the animals were returned to their cages. Grip strength readings were recorded using the manufacturer's software and averaged for each mouse across the five trials.

Cotton swab test

A cotton swab was puffed approximately three times. The puffed cotton swab was applied gently to the plantar surface of the hindpaw for 3 seconds. The response was considered as a paw withdrawal or replacement. The tested paw was alternated after each

Please cite this article in press as: Toscano et al., A spinal circuit for skilled locomotion, Current Biology (2025), https://doi.org/10.1016/j.cub.2025.09.030

CellPress
OPEN ACCESS

application; the initial paw was selected randomly for each animal. A total of five assessments were conducted per animal, with a minimum interval of five minutes between applications to avoid sensitization or habituation effects.

von Frey test

Animals were acclimated to the testing environment for one hour on the day prior to behavioral testing. Paw withdrawal thresholds were then assessed using a standard Semmes-Weinstein set of von Frey filaments (ranging from 0.07 to 4 g; Aesthesio) in accordance with the up-and-down method.[58] A minimum interval of 3 minutes was maintained between consecutive filament applications. The 50% paw withdrawal threshold was determined using the open-source software, up-down Reader (https://bioapps.shinyapps.io/von_frey_app/).

QUANTIFICATION AND STATISTICAL ANALYSIS

The t-tests were performed with GraphPad Prism as unpaired and non-parametric (Mann–Whitney–Wilcoxon). Behavioral data were analyzed with a custom R script using a linear mixed model. Estimated marginal means were calculated to evaluate the effects of group (DT vs PBS) and day (pre vs post). Post-hoc comparisons were performed using effect contrasts to evaluate differences between specific levels of the factors (e.g., pre vs. post) while accounting for variations across groups. Compact letter display was generated to summarize significant differences based on adjusted p-values.[59] To identify the kinematic parameters that contributed to the largest sources of variance in our data, we analyzed 100 parameters extracted from whole-body kinematics during treadmill locomotion and applied principal component analysis (PCA).